[Short title + Author Name - P&H title] 17 (2024) 105680

Contents lists available at ScienceDirect

Arabian Journal of Chemistry

journal homepage: www.ksu.edu.sa

Original article

Effect of red clover (*Trifolium pratense* L.) aqueous extract as an additive on nickel electrodeposition: Experimental and theoretical study

Inam M.A. Omar [a,*], Abdo Mohammed Al-Fakih [b,*]

[a] *Chemistry Department, College of Science, Taibah University, Al Maddinah Al Mounwara, Saudi Arabia*
[b] *Department of Chemistry, Faculty of Science, Universiti Teknologi Malaysia, 81310 Skudai, Johor, Malaysia*

ARTICLE INFO

Keywords:
Plant extract
Electrodeposition
Nickel
Cathodic polarization
Corrosion
DFT

ABSTRACT

Enhancements in nickel electrodeposition have been achieved using organic additives, some of which are not environmentally friendly and may produce undesirable deposits. Red clover leaf extract (RCLE) containing isoflavones was extracted aqueously from the *Trifolium pratense* L. plant. It was used as a green additive for nickel electrodeposition on a copper substrate in an acid-sulfate bath. The mechanism of Ni^{2+} electrodeposition was examined by anodic linear stripping voltammetry, cyclic voltammetry, and cathodic polarization. The surface morphology of the Ni^{2+} coatings were examined using SEM, EDX, XRD, and AFM. The adsorption of RCLE on the Cu substrate inhibited Ni^{2+} deposition and resulted in finer-grained, smoother, more uniform, and stronger hardness deposits. The corrosion protection of nickel coatings in a marine environment containing a 3.5 % NaCl solution was also investigated. The findings demonstrated that the addition of RCLE enhanced the corrosion resistance of Ni^{2+} deposition. The optimal structures of RCLE molecules and their active sites were examined using DFT computations. The results provide concise explanations of the precise atoms and functional groups responsible for the donation and acceptance of electrons. Thus, RCLE showed significant improvements in the process of nickel electrodeposition on a copper substrate in an acid sulfate solution.

1. Introduction

Nickel and its alloys are widely recognized as significant industrial materials owing to their remarkable magnetic, mechanical, chemical, physical and electrocatalytic properties, which qualify them for a diverse range of applications. High levels of heat and corrosion resistance are necessary for the majority of these applications, including chemical, petrochemical, and medical ones as well as power plants, steam turbines, nuclear power plants, and airplane gas (Radadi and Ibrahim, 2021; El-Feky et al., 2013; Omar et al., 2020; Saini et al., 2023). With high hardness and high resistance to tarnish, nickel and its alloys coatings have emerged as viable replacements for chromium coatings in a variety of industries, including the automotive, hardware, electronic and electrical accessory sectors. A highly effective electrocatalyst for the hydrogen evolution reaction (HER) is achieved through the use of a promising nickel (Ni) film. This is primarily attributed to the favorable adsorption strength between Ni and adsorbed hydrogen (Ni-Hads), as well as the greater stability, efficiency, and affordability of Ni and its alloy coatings in comparison to noble metals (Wu et al., 2019; Wang et al., 2019). Additional applications of Ni alloy films include their use in the anode's fabrication for lithium-ion batteries (Radadi and Ibrahim, 2021) and in the development of protein microarray fabrication processes (Chang et al., 2015). Furthermore, nickel deposits find application in other industries such as phonography, printing, tubes, foils, screens, and many others, owing to their advantageous mechanical qualities. Various types of baths such as sulfate, acetate, chloride, sulfamate, citrate, gluconate, and glycine baths, as well as Watts-type nickel baths, with or without additives, have been examined for their potential to deposit nickel (Wojciechowski et al., 2017; Schmitz et al., 2016).

Additives in the electrodeposition process led to more stability, durability and precision for the coating (Deng et al., 2018). An effective role of additives appeared to improve the crystal-building and the surface morphology of the deposit by inhibiting crystal growth of the deposit toward other crystallographic axes (Omar et al., 2020). Additives frequently become a part of the deposit itself and work by adsorbing on the plated surface (Omar et al., 2021). Organic compounds often exert a substantial impact on the degree of adsorption occurring on metal

---

Peer review under responsibility of King Saud University.
* Corresponding authors.
E-mail addresses: emomar@taibahu.edu.sa (I.M.A. Omar), abdo-pd@utm.my (A.M. Al-Fakih).

https://doi.org/10.1016/j.arabjc.2024.105680
Received 12 November 2023; Accepted 9 February 2024
Available online 12 February 2024
1878-5352/© 2024 The Author(s). Published by Elsevier B.V. on behalf of King Saud University. This is an open access article under the CC BY-NC-ND license (http://creativecommons.org/licenses/by-nc-nd/4.0/).

surfaces, therefore making them potentially valuable as efficacious additives. The effectiveness of these organic additives is based on the existence of polar functional groups containing sulfur (S), oxygen (O), or nitrogen (N) atoms within the molecular structure, as well as the existence of heterocyclic compounds (Omar et al., 2021).

Nevertheless, certain additives are not environmentally friendly, such as Cd^{2+} compounds (Mohanty et al., 2002), and thiourea (Zhu et al., 2012) due to high toxicity, high flammability, high volatility, easy decomposition (Ibrahim and Omar, 2013), and low thermal stability (Zhang et al., 2017). Furthermore, the electrodeposition of nickel in the presence of certain organic and inorganic additives demonstrates the formation of granular structures that are characterized by nonuniform characteristics (Guo et al., 2016) with a surface exhibits a significant presence of microcracks (Ibrahim and Al Radadi, 2015; Zhu et al., 2014), low level of hardness and yield strength (Zamani et al., 2016); diminished brightness, reduced resistance to corrosion (Cârâc and Ispas, 2012), inefficient efficiency of cathodic current (Allahyarzadeh et al., 2011), inadequate thermal stability, and limited throwing power (Ibrahim and Al Radadi, 2015). Several additives, such as glycine and sodium citrate, have been employed as additives in the process of electrodeposition of nickel. However, it has been observed that these additives necessitate high current densities and elevated temperature in order to get deposits that are free from cracks (Guo et al., 2016).

The harmful effects associated with synthetic organic additives and the implementation of strict environmental restrictions have prompted researchers to shift their attention towards the development of affordable and environmentally friendly natural materials for use as additive agents in electrodeposition processes. These organic substances that are naturally occurring are either extracted or produced from medicinal plants, fragrant herbs, and spices. Plant extracts are thought to be an extraordinarily abundant source of chemical compounds that are spontaneously generated, easily extracted, inexpensive, and biodegradable (Hanini et al., 2019; Zaabar et al., 2020; Karima et al., 2021). Many green plant extracts can be biodegradable and may not typically contain heavy metals or other toxic compounds. The use of plant extracts as additives in electrodeposition has become important because they are environmentally acceptable, readily available, and renewable sources for a wide range of green additives (Hanini et al., 2019; loto et al., 2020). loto, Loto and Akinyele (loto et al., 2020) reported that natural extracts from ginger, pomegranate, and celery demonstrate practical with excellent results when used as additives in the zinc electroplating process for mild steel. Zaabar, Rocca, Veys-Renaux, Aitout, Hammache, Makhloufi and Belhamel (Zaabar et al., 2020) investigated the process of depositing zinc from an acidic sulphate solution in the presence of nettle extract at room temperature. The study revealed that the inclusion of nettle extract modifies both the electrochemical properties of zinc electrodeposition and the characteristics of the resulting zinc deposit. El Sayed and Ibrahim (El Sayed and Ibrahim, 2019) incorporated natural kermes dye (NKD) as an additive in the electrodeposition of nickel from a Watts-type nickel bath. The study revealed significant enhancements in both the corrosion resistance and microhardness of the resulting nickel electrodeposits. Loto and Loto (Loto and Loto, 2013) examined the impact of adding nicotiana tobaccum (tobacco) extract to the electrodeposition process of zinc on mild steel in an acid chloride solution. The study revealed that the utilization of tobacco extract as an additive resulted in favorable zinc electrodeposition, characterized by fine, dense, and closely packed crystal grains on the surface of mild steel in the acidic zinc chloride solution. Loto, Olofinjana and Popoola (Loto et al., 2012) explored the process of zinc electrodeposition on mild steel in an acid chloride solution, employing sugarcane (Saccharum officinarum) juice as the additive. This approach resulted in successful zinc electrodeposition on the surface of mild steel.

In an effort to enhance the quality of Ni deposition and address the limitations associated with additives in Ni electrodeposition, this study investigates the use of *Trifolium pratense* L., commonly known as red clover leaf extract (RCLE), as a green additive. The chemical structures of isoflavones components are shown in Fig. 1. Our hypothesis suggests that isoflavones function as the major active constituents in red clover leaf extract. This hypothesis comes from the idea that isoflavones are the main parts of the extract, possessing both oxygen heteroatom and π electrons. These constituents play a crucial role in surface phenomena during the electrochemical deposition of nickel, promoting the formation of finer-grained, smoother, more uniform, and harder deposits through adsorption. The presence of oxygen heteroatom and π electrons in isoflavones aligns with and substantiates our proposed mechanism (Alesary et al., 2020; Zou et al., 2023).

In the present work, RCLE (*Trifolium pratense* L.) was evaluated as a green additive for Ni electrodeposition on a copper substrate. The additive should have the ability to adsorb onto the electrode surface, influencing the nucleation and growth of the metal crystals (Omar et al., 2021; Juma, 2021). Isoflavones are potential advantageous additives in Ni electrodeposition due to their adsorption characteristics. The chemical structures of the isoflavones involve the oxygen atom as a heteroatom, π electrons, and functional groups such as methoxy and hydroxyl. Thus, the adsorption of the isoflavone additives on the electrode function as inhibitors of hydrogen evolution, helping to reduce the formation of hydrogen gas during electrodeposition (Omar et al., 2021; Juma, 2021).

In order to clarify the behavior of electrodeposition and the process of nucleation for nickel thin films derived from acidic sulfate in the presence of RCLE, several experimental and theoretical measurements were conducted. The experimental techniques employed in this study encompassed cathodic polarization, anodic linear stripping voltammetry (ALSV), and cyclic voltammetry (CV). Analysis was also done on the surface morphology of the produced nickel film. DFT quantum calculations were also used to gain insight regarding the active sites and electronic interactions that occur between the examined RCLE additives and the copper surface. To the best of our knowledge, the process of nickel electrodeposition in the presence of RCLEs have not been previously reported in the literature as additives.

2. Experimental details

2.1. Plant extract preparation

The leaves of the selected red clover plant were harvested from local farms located in Madinah in the KSA. Fresh leaves of red clover plants were removed from the plants. The leaves were washed under running tap water to remove dust and were then rinsed with distilled water. After that, the leaves were shade dried at room temperature (25 °C) for two weeks, and finely powdered plant materials were stored in polythene bags in the dark to protect them from sunlight until use. In brief, an aqueous extract of RCLE was prepared as follows. Red clover leaf powder was extracted by mixing 10 g with 300 ml distilled water in a 500 ml

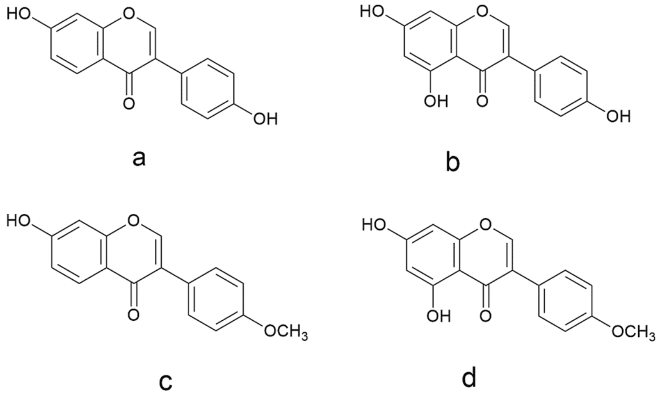

Fig. 1. Chemical structures of an active isoflavone; (a) Daidzein, (b) genistein, (c) formononetin, and (d) biochanin A of RCLE.

standard beaker. The mixture was boiled for one hour until the total volume decreased to half. Thereafter, the mixture was left to cool at room temperature for half an hour, and then it was decanted and filtered by centrifugation for 20 min at 5000 rpm (HERAEUS LABOFUGE 200, GERMANY). The solution undergoes filtration in order to remove any remaining residues (Kazlauskaite et al., 2021; Kazlauskaite et al., 2021; Kazlauskaite et al., 2022). The clear RCLE solution (100 ml) was stored in a dark stock to be used as a green aqueous extract additive during Ni electrodeposition. According to the literature, isoflavones were extracted from *Medicago* species through various extraction procedures, including aqueous extraction method (Rodrigues et al., 2014).

2.2. *RCLE characterization*

The characterization of RCLE was conducted in previous studies (Gościniak et al., 2023; Lemežienė et al., 2015; Saviranta et al., 2008). The composition and content of active compounds were evaluated using the high-performance liquid chromatography (HPLC). RCLE was found to contain four common active isoflavone ingredients, including daidzein, genistein, formononetin and biochanin A, exhibiting the highest concentrations in the extract, as reported in (Lemežienė et al., 2015; Saviranta et al., 2008). Therefore, this work focuses on these isoflavones, with their chemical structures illustrated in Fig. 1.

2.3. *Electrodeposition fabrication*

The process of electrochemically depositing nickel onto a copper substrate with a purity of 99.9 % was carried out from sulfate baths containing RCLE (Table 1) via many techniques. The concentration of RCLE in the Ni electrodeposition bath is represented as a percentage. The amount of RCLE (μL) per 50 × 10^3 μL of Ni electrodeposition bath and the percentage of RCLE in the Ni electrodeposition bath are listed in Table T1. A deposition cell in the form of a rectangular trough was utilized. Prior to each experiment, the copper sheets underwent a cleaning process involving immersion in a pickling solution consisting of 300 ml of sulfuric acid (H_2SO_4), 100 ml of nitric acid (HNO_3), 5 ml of hydrochloric acid (HCl), and 595 ml of water (H_2O) for a duration of 20 s. Subsequently, the sheets were rinsed with distilled water and then dried in a desiccator. All chemicals and reagents were of analytical grade, and fresh electrolytes were made with double-distilled water. A pH meter was used to measure the pH and modify it using a 1:1 (H_2SO_4: H_2O) ratio (HANNA, IH 2210, ITALY).

Table 1
The constituents of the bath, experiment settings/parameters, and the electrodes used for Ni electrodeposition.

Electrolyte (Watts) solution composition	g/L
$NiSO_4 \cdot 6H_2O$ (source for Ni)	165.60
$NiCl_2$ $6H_2O$ (source for Ni)	17.02
H_3BO_3(buffer)	30.00
RCLE (additive)	5–500 μL
Operating conditions	
Current density (mA/cm^2)	6–24
pH	4.5
Temperature (°C)	25
Electrodes	
Cathode	Cu sheet (6.25 cm^2, 0.25 cm thick, 99.99 %, Advent Research Materials)
Anode	Pt sheet 6.25 cm^2, 0.25 cm thick, 99.95 % metals basis. Alfa Aeser.
Working electrode (WE)	Glassy carbon electrode (GCE) (0.156 cm^2 Glassy carbon disk electrode in peek body 6 mm Reorder ET 051)
Counter electrode (CE)	Pt sheet 6.25 cm^2, 0.25 cm thick, 99.95 % metals basis. Alfa Aeser.
Reference electrode (RE)	Saturated calomel electrode (SCE), (Hanna Instrument (Italy) HI5412)
The deposition cell	A rectangular trough (10 × 2.5 × 2 cm, made by Perspex).

2.4. *Electrochemical setup*

The process of cathodic electrodeposition was applied to deposit nickel (Ni) onto a flat copper (Cu) substrate, while a platinum (Pt) sheet of equal dimensions was utilized as the anode. Direct current was supplied utilizing a QJ3005A DC power supply unit under various conditions, as outlined in Table 1. A Gamry potentiostat/galvanostat (specifically, the Gamry Interface 1000) connected to a PC was used to run the electrochemical experiments on a three-electrode cell. The data obtained from these experiments were subsequently processed using the Gamry Echem software. The counter electrode (CE) was platinum (Pt), whereas the reference electrode (RE) was a saturated calomel electrode (SCE). A copper sheet or glassy carbon electrode (GCE) was employed as the working electrode (WE) in accordance with the established methodologies. Prior to each run, the GCE underwent a polishing process utilizing alumina slurry till achieving a shiny finish. Potentiodynamic cathodic polarization curves were generated by employing a copper sheet as the working electrode (WE). The potential was systematically varied from the rest potential towards less noble potentials, ranging from -0.5 V_{SCE} to -1.5 V_{SCE}, at a scan rate of 10 mVs^{-1}. Cyclic voltammetric (CV) measurements were conducted utilizing a Glassy Carbon Electrode (GCE) as the Working Electrode (WE) within a potential range of 0.5 V_{SCE} to -1.5 V_{SCE}, employing a scan rate of 100 mVs^{-1}. In the context of in situ anodic linear stripping voltammetry (ALSV) measurements, the process of Ni deposition was conducted on the GCE at a constant potential of -1.0 V_{SCE}. This deposition was performed for a fixed duration of 100 s at a temperature of 25 °C. After each deposition period, an in-situ stripping analysis was conducted promptly within the same plating bath. This involved sweeping the potential from -0.5 V_{SCE} to higher anodic potentials (0.2 V_{SCE}) at a sweep rate of 10 mV s^{-1}, without removing the working electrode from the solution (El Sayed and Ibrahim, 2019).

2.5. *Surface morphology*

The morphology of the Ni thin films was examined using a scanning electron microscope (SEM) equipped with an energy dispersed X-ray spectrometer (EDX). The SEM used for this study was a JEOL JSM-6000 model manufactured by Shimadzu in Japan. The microanalysis hardware of the SEM was operated at a voltage of 15 kV. The phase identification of the Ni films that were made was conducted using X-ray diffraction (XRD) analysis. The XRD instrument used was a Shimadzu XRD-7000 from Japan, which utilized monochromatic Cu kα radiation of 1.5406 A°. The XRD analysis was performed at an operating voltage of 40 kV and a current of 30 mA, with a 2θ angle pattern. The evaluation of the topography and roughness of the deposited films was carried out via atomic force microscopy (AFM) employing the (Veeco digital equipment CP-II, contact mode). The measurement of Ni deposit hardness was conducted by performing Vickers microhardness tests using the (Hysitron TI 725 Ubi. Model, USA). A load of 25 g-force was applied for a duration of 60 min. Indentations were created on the surface of the plates in a parallel manner to the base metals. A set of five measurements was obtained by taking readings at various points along the circumference of a circle. These measurements were then used to determine the microhardness of each sample. The findings were reported in terms of Vicker's hardness number (V.H.N.).

2.6. *Corrosion resistance measurements*

In order to assess the corrosion resistance of the nickel coatings in a marine environment (3.5 % NaCl solution) at 25 °C, various electrochemical measurements were conducted. These measurements included open-circuit potential (OCP) testing, electrochemical impedance spectroscopy (EIS), and potentiodynamic polarization. In this context, electrochemical investigations were conducted using a three-electrode corrosion cell. The experimental setup involved the utilization of a Pt sheet as the counter electrode (CE), an SCE as the reference electrode (RE), and samples with deposited Ni as the working electrode (WE). The initial step involved immersing all samples in a 3.5 % NaCl solution for a duration of roughly 30 min in order to establish a stable open circuit potential (OCP). The EIS measurements were conducted within the frequency range spanning from 100 kHz to 0.01 Hz. A voltage amplitude of 10 mV was superimposed on an alternating current (AC) signal during the experiments. Subsequently, the matching Nyquist plots were acquired. After that, potentiodynamic curves were obtained through the process of scanning within the range of ± 700 mV from the OCP, with a scan rate of 1 mV.

2.7. Quantum chemical calculations

The molecular structures of RCLE additives were depicted utilizing Chem3D software. The optimization of the geometry and calculation of the quantum chemical parameters for the investigated RCLE additives were performed using the Gaussian09 (Frisch et al., 2009) program. This was carried out at the B3LYP level of density functional theory (DFT) with the 6–311++G(d,p) basis set. The natural atomic charge, E_{HOMO}, E_{LUMO}, ΔE, electron affinity (A), ionization potential (I), electronegativity (χ), softness (S), hardness (η), and the fraction of electrons transported from the inhibitor to the metal surface (ΔN) were computed. The quantum chemical computations were performed in the gas phase. The following equations (Eqs. (1)–(7) were used to calculate the values of the quantum parameters.

$$\Delta E = E_{LUMO} - E_{HOMO} \tag{1}$$

$$I = -E_{HOMO} \tag{2}$$

$$A = -E_{LUMO} \tag{3}$$

$$\chi = -\frac{1}{2}(E_{HOMO} + E_{LUMO}) \tag{4}$$

$$\eta = -\frac{1}{2}(E_{HOMO} - E_{LUMO}) \tag{5}$$

$$S = \frac{1}{\eta} \tag{6}$$

$$\Delta N_{max} = \frac{x}{2\eta} \tag{7}$$

3. Results and discussion

3.1. Cathodic polarization

The significance of cathodic polarization (CP) curves is in their ability to provide insights into the mechanisms of electrodeposition and to evaluate the impact of RCLE additives on the electrodeposition process. Fig. 2 exhibited typical cathodic polarization (CP) curves recorded during Ni electrodeposition from an RCLE-free solution and a solution containing RCLEs at pH 4.5. The potential of the cathodic curves was swept between −0.4 and −1.5 V_{SCE}. Nickel deposition from a RCLE-free aqueous solution is accompanied by high polarization. The electrodeposition reactions of Ni^{2+} ions from the RCLE-free system occurred under an electrical field at 25 °C through a direct reduction mechanism, as shown in Eq. (8). The mechanism of the metal ion reduction reaction from an aqueous bath is explained in detail in (Santos et al., 2007).

$$Ni^{2+} + 2e \rightarrow Ni \tag{8}$$

$$2H^{+} + 2e \rightarrow H_2 \tag{9}$$

Moreover, the hydrogen ions simultaneously released as a side-reaction during the deposition of the Ni^{2+} ions (Eq. (9). Generally, the mechanism of the hydrogen evolution reaction (HER) is performed in three steps, the Volmer, Tafel, and Heyrovsky steps (Anand Raj and Arumainathan, 2019). Fig. 2 shows the overpotential of Ni depositions in overpotential regions marked from the equilibrium potential, −0.4 V, to − 0.9 V, which represents the Volmer step for hydrogen adsorption (Eq. (10); from − 0.9 V to − 1.3, which represents the Tafel step for hydrogen evolution (Eq. (11); and from − 1.3 to above, which represents the Heyrovsky step for hydrogen evolution (Eq. (12) (Anand Raj and Arumainathan, 2019).

$$\text{Volmer step}: \quad H^{+} + e \rightarrow H_{ads} \tag{10}$$

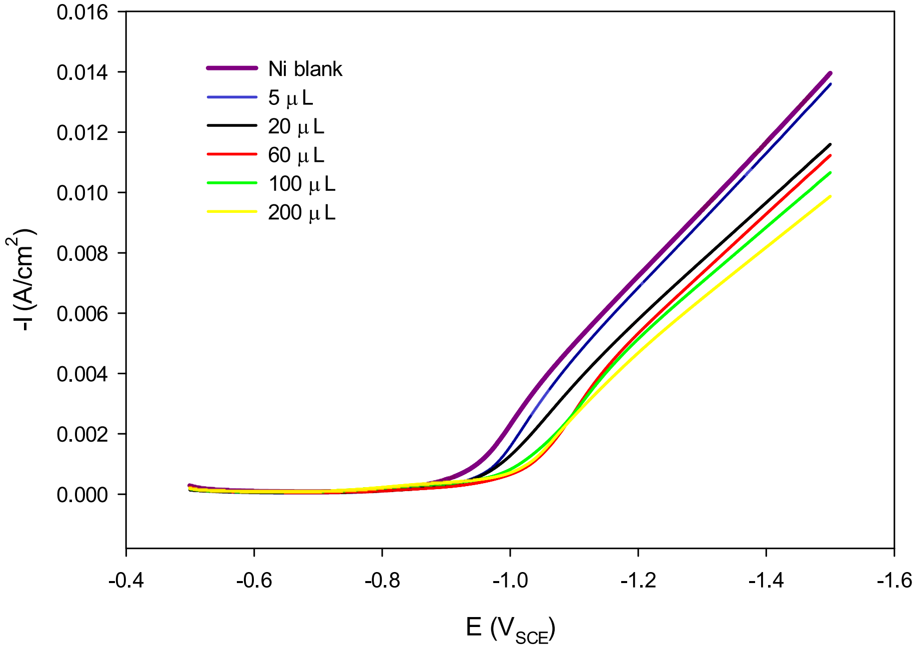

Fig. 2. Potentiodynamic cathodic polarization (CP) curves for Ni electrodeposition in the absence (blank) and presence of RCLE at pH 4.5.

$$\text{Tafel step}: \quad 2H_{ads} \rightarrow H_2 \tag{11}$$

$$\text{Heyrovsky step}: \ H_{ads} + H^+ + e \rightarrow H_2 \tag{12}$$

The identical form and polarization characteristics were observed in both the absence and presence of RCLE in the Ni electrodeposition baths, i.e., the activation polarization remained unchanged. The presence of RCLE resulted in a clear shift in the polarization curves towards more negative overpotential values and a noticeable drop in cathodic current, suggesting the inhibition of the electrodeposition of Ni^{2+} ions. Furthermore, an evident shift in the cathodic polarization potential (CPP) toward less noble potentials was observed in the presence of RCLE. The inhibitory impact of RCLE is ascribed to its adsorption on the metal surface. These adsorption processes increased the overpotential by reducing the available sites for the discharge of Ni^{2+} ions (Ibrahim and Omar, 2013; Zhang and Hua, 2009). A change in the CPP for nickel electrodeposition was detected when a current density of 5.0×10^{-3} mA cm^{-2} was applied. The CPP shifted from -1.03 V_{SCE} to -1.12 V_{SCE} in the presence of 100 μL of RCLE, as shown in Table T2. The enhancement of the inhibitory effect of RCLE was observed as the additional volume increased (Fig. 2), as evidenced by the high CPP values (Table T2). The observed decrease in the cathodic current, accompanied by a shift towards more negative cathodic potential, suggests that the presence of RCLE inhibits the electrodeposition of Ni^{2+} ions, i.e., the obtained results indicate that the presence of RCLE has an inhibiting effect on the kinetics of the Ni discharge process. In the presence of RCLE, the concentration of H_{ads} (Eq. (10) and the rate of hydrogen evolution (Eq. (9) exhibit a reduction. The observed inhibitory impact of the investigated RCLE can be ascribed to its simultaneous adsorption on the surface of the copper substrate (Ibrahim and Omar, 2013).

RCLE contains four active isoflavone ingredients (daidzein, formononetin, genistein and biochanin A), as shown in Fig. 1. The adsorption mechanism of four active isoflavone ingredients in RCLE can be justified based on their molecules. The phenomenon of simultaneous adsorption of four isoflavone molecules is ascribed to the existence of several active sites for adsorption. The active centers in the four isoflavone chemical structures are particularly located in the functional groups, as shown in Fig. 1. The isoflavone structures of daidzein, genistein, formononetin, and biochanin A consist of three functional groups. One oxygen atom is a heteroatom that has a lone pair of electrons. The carbonyl functional groups are characterized by the presence of oxygen atoms and 2p-electrons. In the chromen-4-one structure, there are eight p-electrons resulting from four conjugated double bonds, whereas in the phenyl ring, there are six p-electrons. One or two hydroxy functional groups, characterized by the presence of oxygen atoms. The methoxy functional group is characterized by the presence of a single oxygen atom. Aromatic rings with p-electrons can be better adsorbed on the cathode surface and can consequently increase the polarization of the Ni electroplating (Omar et al., 2021). Generally, when the quantity of double bonds grows, there is a corresponding increase in the number of p-electrons. Consequently, the process of adsorption on the cathode surface is facilitated (Deng et al., 2018). Moreover, oxygen atoms in the four isoflavone chemical structures have the property of electron donation, which is associated with a strong adsorption ability on the surface of the metal (Pramod Kumar et al., 2019). Based on the preceding explanations, it can be concluded that the application of an electrical current to a WE result in the attraction and adsorption of RCLE molecules onto the electrode's energetically favorable surfaces, characterized by low energy. Consequently, this process restricts the availability of high energy surfaces for the deposition of metal ions (Bani Hashemi et al., 2017). The presence of the four active isoflavone components of RCLE results in the creation of a network on the electrode surface, hence impeding the growth of sizable nickel crystals. The current evidence suggests that adsorption processes have the effect of increasing the overpotential by reducing the number of sites accessible for the discharge of Ni^{2+} ions (Ibrahim and Omar, 2013). In other words, the rate of deposited ion transfer across the electrical double layer is slowed down by RCLE molecules.

3.2. Tafel lines and electrode kinetics

Cathodic polarization curves developed under strictly controlled conditions provide valuable insights on coatings, passivity, films, and kinetics. As above elucidated, the application of electrical current induces the evolution of hydrogen gas at the cathode within an acidic solution, thereby competing with the reduction process of Ni^{2+}. The computed electrochemical kinetic variables regarding the mechanism of hydrogen reduction during Ni electrodeposition in the presence of RCLE additives can be obtained from polarization measurements (Fig. 2). The cathodic current densities, i_c, for the nickel deposition were obtained using the extrapolation of the Tafel lines to a zero overpotential. The cathodic Tafel slope (b_c), transfer coefficient (α_c), and cathodic current density (i_c) are determined by utilizing the Tafel equation, as denoted by Eq. (13).

$$\eta_c = a + b_c \log i_c \tag{13}$$

Eq. (14) is used to ascertain the transfer coefficient (α_c).

$$b = RT/\alpha nF \tag{14}$$

where R and F are the gas constant and Faraday's constant, respectively, and n is the number of electrons (Omar et al., 2020). The results given in Fig. S1 and Table 2 specify that b_c increases and α_c decreases gradually during nickel reduction when RCLE was included in the bath. This decrease in α_c values corresponds to variations in the morphological features of the nickel deposits (Ibrahim and Omar, 2013); as shown in Fig. 4. As depicted in Table 2, the i_c exhibited an increase, transitioning from -0.874 Acm^{-2} in the absence of RCLE to -0.891, -0.899, and -0.929 Acm^{-2} in the presence of 5, 20, and 60 μL of RCLE, respectively. Generally, i_c tends to increase when the electrochemical process is inhibited (Omar et al., 2020). The results of this study suggest that the transfer of Ni^{2+} ions across the electric double layer is hindered as a result of rapid adsorption of RCLE onto energetically favorable sites on the metal electrode, which are characterized by low energy surfaces. Consequently, only the high energy surfaces of the metal electrode remain available for the deposition of Ni^{2+} ions onto the metal surface (Omar et al., 2021). The inclusion of an adsorbate has the potential to modify the structure of the double layer and thus impede the rate of an electrochemical reaction (El Sayed and Ibrahim, 2019). At concentrations higher than 60 μL, there are no significant changes in i_c. This lack of variation may be attributed to the saturation of the metal surface.

3.3. Adsorption isotherms

Adsorption isotherms gives valuable insights into the nature of the interaction between additives and metal deposits. The various adsorption isotherms can be determined based on the potentiodynamic cathodic polarization curves obtained during the process of Ni^{2+} electrodeposition. The data were fitted with Langmuir and Temkin adsorption isotherms according to Eqs. (16–18). The calculation of the surface coverage (θ) for the adsorbed RCLE component additive can be derived using Eq. (15) (Ibrahim and Omar, 2013):

Table 2
Tafel kinetic parameters obtained for Ni different plating solutions.

RCLE (μL)	b_c (mV decade^{-1})	i_c (Acm^{-2})	α_c
0	−44.9760	−0.874	2.854e-4
5	−45.1825	−0.891	2.842e-4
20	−50.7161	−0.899	2.531e-4
60	−51.8048	−0.929	2.479e-4
100	−54.3605	−0.918	2.362e-4
200	−57.4287	−0.929	2.235e-4

$$\theta = (1 - i_{add}/i) \tag{15}$$

where i_{add} and i represent the current density for Ni electrodeposition at a constant potential (-1.2 V_{SCE}) with and without the RCLE additive components, respectively. The θ value expands with increasing RCLE concentration for Ni^{2+} depositions, as shown in Table T2, which indicates a greater adsorption rate for the four isoflavone ingredients in RCLE on the cathode surface.

3.3.1. Langmuir adsorption isotherm

Fig. S2.a shows that the data were fitted using the Langmuir adsorption isotherm, Eq. (16) (Ibrahim and Omar, 2013):

$$\theta/1 - \theta = K[C] \tag{16}$$

where **C** is the concentration of RCLE in the bulk of the solution and **K** represents the equilibrium constant of the adsorption reaction. A great $K_{Langmuir}$ value of 1753.767 M^{-1} for the Ni^{2+} bath is displayed in Fig. S2.a. Table 3 shows a highly favorable adsorption process for a particular compound, meaning that the adsorbing molecules and the double layer at the phase boundary have greater electrical interactions. The ΔG°_{a} value was determined to be −28.41 kJ mol^{-1} indicating a spontaneous adsorption of RCLE isoflavones onto the Cu surface and falls within the anticipated ranges for chemical and physical adsorption (Gholami et al., 2013; Deng et al., 2011; Ahamad et al., 2010; Aribou et al., 2023). This indicates that the adsorption of the four active isoflavone ingredients in RCLE involves both physical and chemical adsorption (mixed type). The obtained result demonstrates a strong correlation with the high overpotential found in the cathodic polarization curves during the process of nickel electrodeposition in the presence of RCLE. Comparable findings have been documented in the case of ionic liquids and organic compounds (Omar et al., 2021).

3.3.2. Temkin and Flory–Huggins adsorption isotherms

The Temkin adsorption isotherm model is expressed according to Eq. (17) (Emran et al., 2015):

$$\theta = \frac{-2.303 logK}{2a} - \frac{2.303 logC}{2a} \tag{17}$$

where **K** is the adsorption equilibrium constant and **a** is the attraction parameter. The adsorption of RCLE ingredients is fitted by the Temkin adsorption isotherm, as confirmed via the linear relationship between **θ** and log [RCLE] in Fig. S2.b. The value of **a** is negative (Table 3), indicating that repulsion exists between adsorbed RCLE molecules and that there are no interactions among them, as reported in (Emran et al., 2015). A high value of K_{Temkin} (Table 3) indicated a strong adsorption of RCLE components molecules on the Cu surface.

Furthermore, the Flory–Huggins adsorption isotherm model is expressed in Eq. (18) (Emran et al., 2015).

$$log\frac{\theta}{C} = logK + xlog(1 - \theta) \tag{18}$$

where **θ** is the surface coverage, **C** is the additive concentration, **K** is the adsorption equilibrium constant, and x is the number of additive molecules occupying one site. Fig. S2.c shows a linear relation between log θ/C and log (1-θ), indicating that the data fit the Flory–Huggins adsorption isotherm model (Emran et al., 2015). Table 3 illustrates that the values of x during Ni^{2+} electrodeposition were 4.66≈5, which means that one molecule of RCLE replaced 5 water molecules. On the other hand, the values of the linear correlation coefficient (r^2) in Table 3 show a closer proximity to 1 for the Langmuir and Temkin isotherm models in comparison to the Flory–Huggins model. This suggests that the adsorption of RCLE ingredients on the Cu surface is better represented by the Langmuir and Temkin adsorption isotherm models.

Table 3
Adsorption isotherm parameters of RCLE adsorption on Cu substrate during Ni electrodeposition.

Isotherm	K	Parameter	r^2
Langmuir	1753.77	ΔG^{o}_{a} = -28.41 kJ/mol	0.9789
Temkin	446262.10	a = -6.3288	0.9799
Flory-Hoggins	16319.68	x = 4.66	0.8004

3.4. Cyclic voltammetry

Cyclic voltammetry (CV) was used to elucidate the reduction potential regions and qualitatively characterize the metal deposition processes under different conditions (Sorour et al., 2017). As shown in Fig. 3.a, the cyclic voltammograms were obtained by conducting experiments on GCE to evaluate the electrodeposition of Ni^{2+} from an acidic sulfate solution. The experiments were conducted both in the absence and presence of RCLE at concentrations ranging from 5 to 500 μL with potential range from 0.5 to −1.5 V_{SCE}, and a scan rate of 100 mV s^{-1}. Ni^{2+} electrodeposition began at ∼ −0.9 V_{SCE}, point A, while the cathodic peak current was recorded at −1.5 V_{SCE}, point B, for all CVs. A dramatic growth in the cathodic current was recorded for Ni^{2+} deposition with metallic light silver deposits with the coevolution of H_2 when the scan proceeded toward more negative potentials (>-1.0 V_{SCE}) between points A and B. The coevolution of H_2 was seen when H_2 gas bubbles appeared at the edge of the deposited layer on the GCE at potentials more negative than −1.4 VSCE. However, the cathodic peak currents for Ni^{2+} reduction dropped sharply from −0.0113 A cm^{-2} for the RCLE-free solution to −0.0033 A cm^{-2} for the solution containing 500 μL RCLE. The observed phenomenon of the inhibition of Ni^{2+} electrodeposition with increasing RCLE concentration can be attributed to the adsorption of RCLE ingredients molecules on the active sites that possess low energy on the cathode surface. It also depends on the depletion of Ni ion concentration in the electrolyte near the cathode surface. Therefore, the current flow is primarily governed by the diffusion of Ni^{2+} ions from the electrolyte to the cathode surface. This demonstrates how the dispersion of Ni cations influences Ni deposition. The current drops on the reverse scan and reaches zero at point C, the crossover potential (-0.5 VSCE). As can be seen in Fig. S1 a, the current then becomes anodic, which corresponds to the cathodically deposited Ni's dissolution at point D. The anodic scan revealed a very low oxidation current, suggesting that the Ni electrodeposit is not easily dissolved in the bath. This finding demonstrates how strongly nickel deposits adhere to copper (Nemţoi et al., 2009).

Further information regarding the extent of polarization of the cathode could be obtained by calculating the nucleation overpotential (NOP) from CVs (Table T2). NOP was calculated by considering the difference in reduction potential between point A and the crossover potential (i = 0 Acm^{-2}, E = -0.6 V_{SCE}) at point C. Strong polarization and inhibition of the electrodeposition process were confirmed by increasing the NOP values with increasing RCLE concentration in the bath, as shown in Table T2 (Omar et al., 2020). This is attributed to the θ of the cathode by strongly adsorbed isoflavone ingredients in RCLE, which blocks the active sites available for Ni deposition. This result confirms the previously obtained results, which include a significant change in the cathodic polarization curves toward a more negative potential and high values of $K_{Langmuir}$, ΔG, and CPP.

Fig. 3.b represents the impact of the scan rate on the electrodeposition behavior of nickel in the presence of 5 μL of RCLE. The shift of Ni reduction peaks to more negative potentials and the corresponding rise in current contribution with increasing scan rate elucidate the qualitative impact of scan rate on the electrodeposition process. When the nucleation overpotential rises with the scan rate, a current crossover also happens in the cathodic branches, suggesting a typical nucleation process for deposition. According to Omar, Emran, Aziz and Al-Fakih (Omar et al., 2020), the Randles-Sevcik equation demonstrates the electrochemical behavior of an irreversible process in a diffusion-

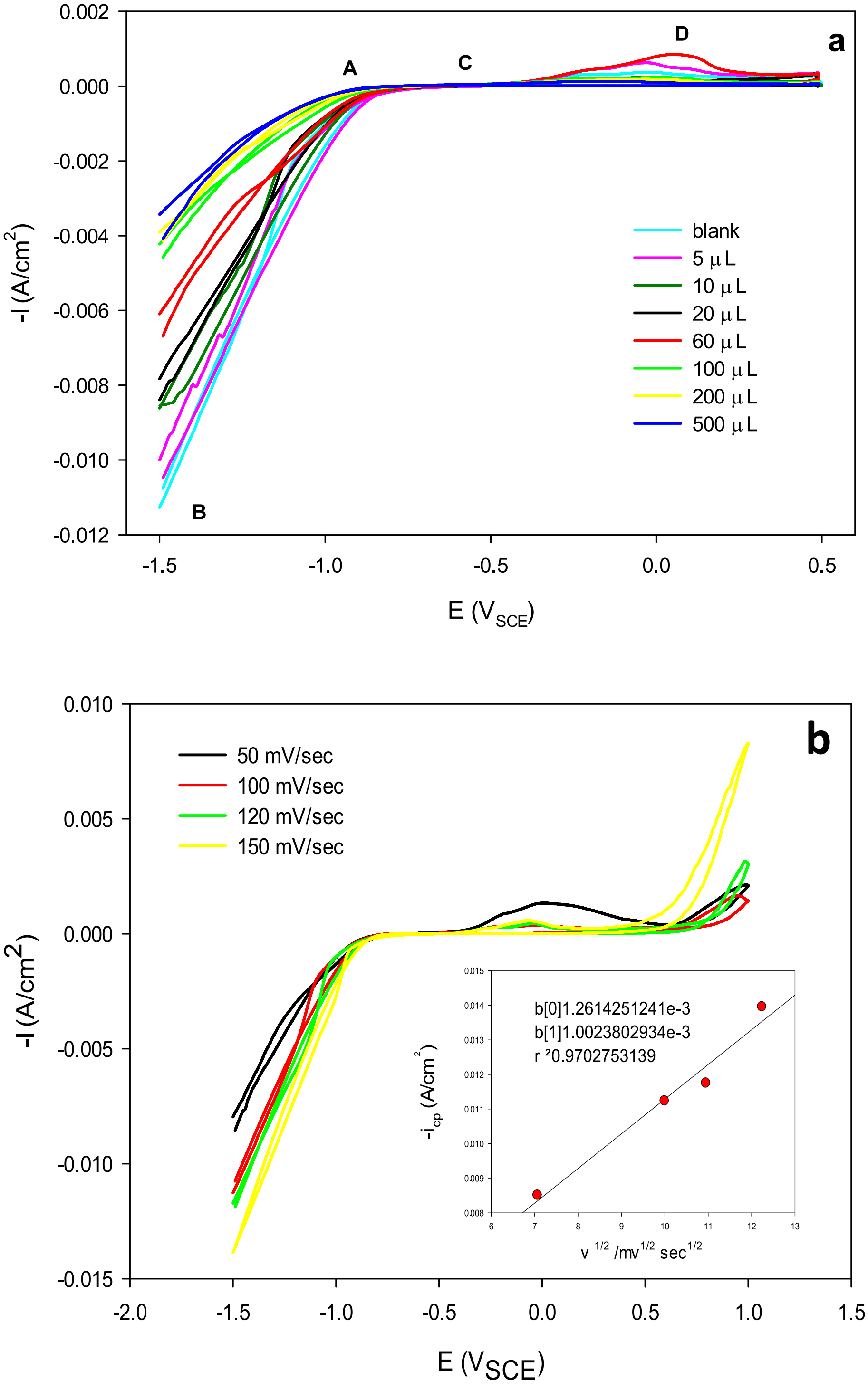

Fig. 3. (a) CVs Ni electrodepositions acquired at 100 mV/sec scan rate at GCE with and without RCLE. (b) Ni electrodeposition CVs measured at GCE with varying scan rates at 5 μL RCLE. The R-S plot's inset shows the linear relationship between the cathodic peak current density (i_{cp}) and the scan potential rate ($\nu^{1/2}$).

controlled system. The observed linear relation between i_{cp} and $\nu^{1/2}$, as depicted in Fig. 3.b, implies that the rate of growth is influenced by the mass transport of Ni^{2+} ions to the growing center. Recent studies have documented comparable electrochemical findings in the presence of imidazole ionic liquid additives (Omar et al., 2020; Omar et al., 2021) and ninhydrin organic additive (Ibrahim and Omar, 2013).

3.5. *Anodic linear stripping voltammetry (ALSV)*

Anodic linear stripping voltammetry (ALSV) measurements can provide the composition, phase and anodic behavior of Ni deposits, as well as the quantitative determination of specific ionic species. After deposition of Ni^{2+} onto a GCE at −1.0 V_{SCE} for 100 sec, the anodic stripping of Ni was initiated with the onset of the anodic sweep at −0.6 V_{SCE} for Ni (Fig. S3). The anodic current density increased with increasing potential to reach a maximum, as shown in Table T2. Then, the current density decreased steeply at more anodic potentials (1.0 V_{SCE}) at a scan rate of 20 mV s^{-1}. It is clear that Ni^{2+} generated in the anodic process interacted with proper anions present in the baths. A protective layer at the metal/electrolyte interface was formed, which

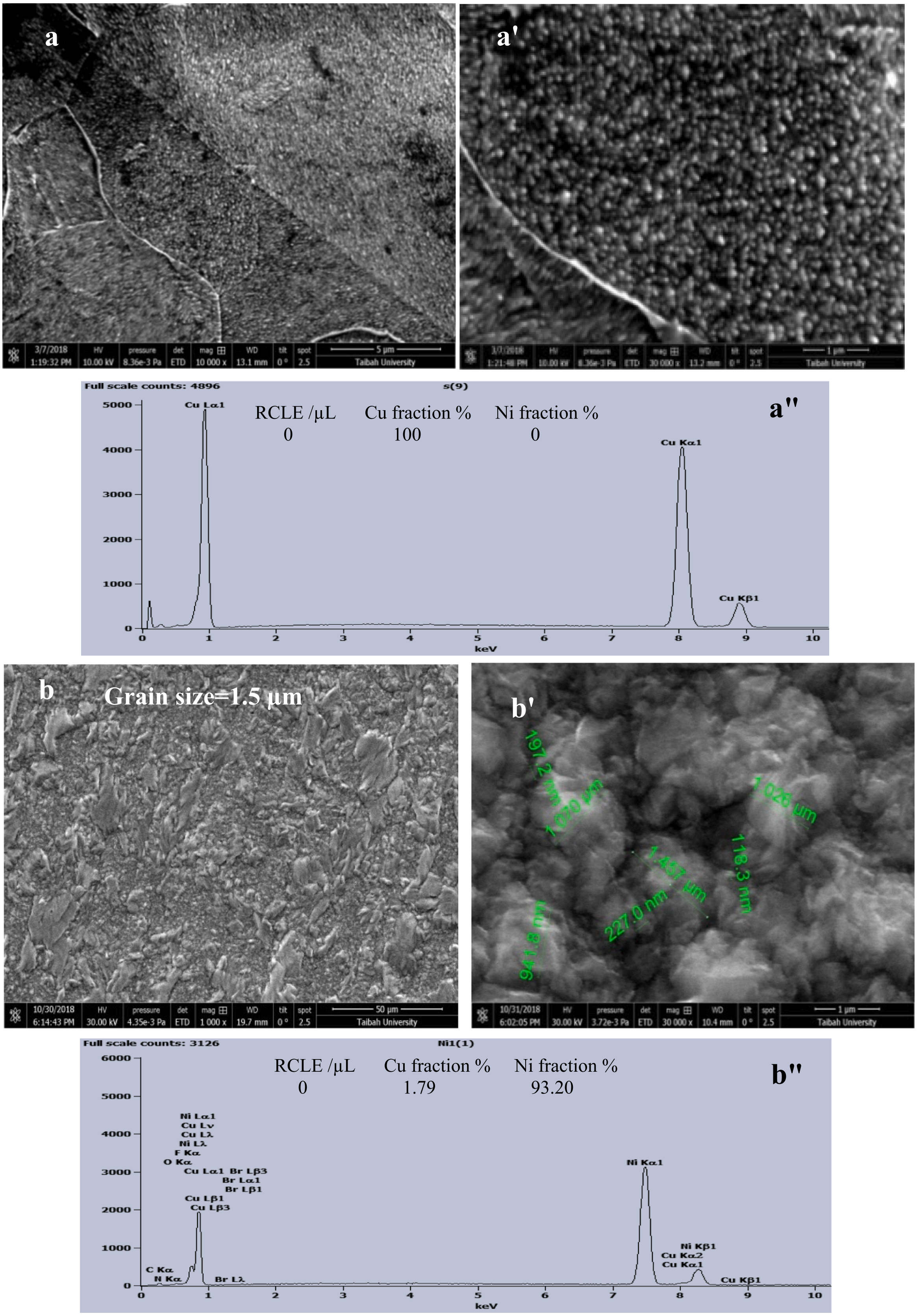

Fig. 4. SEM images, high magnification SEM and EDX spectra of Ni deposits (a, a', a") Cu substrate, (b, b', b") in RCLE-free bath, (c, c', c") 60 μL RCLE, (d, d', d")100 μL RCLE.

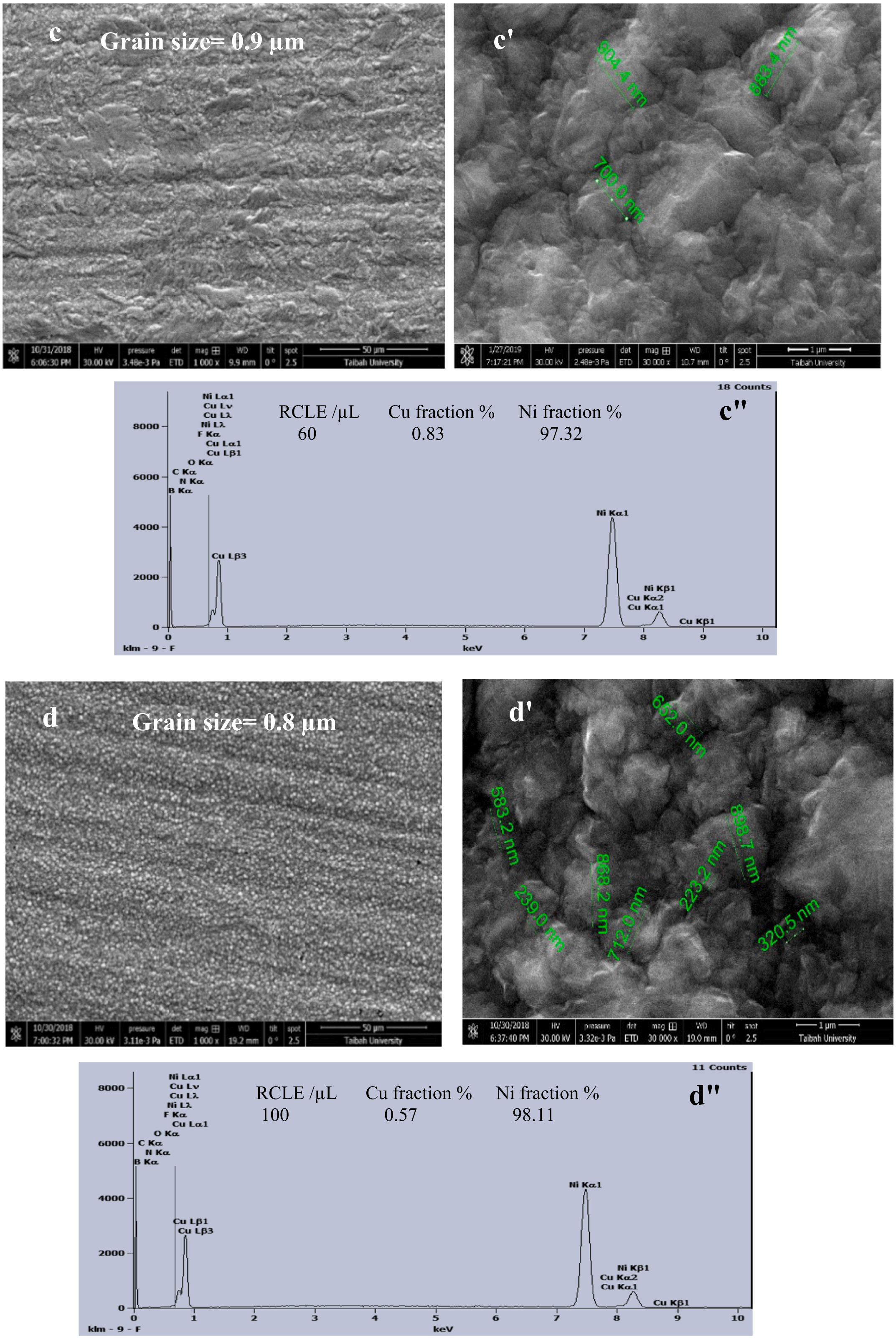

Fig. 4. (*continued*).

inhibited further anodic dissolution of Ni at potentials higher than 0.2 V_{SCE}. Fig. S3 shows the effect of RCLE on the ALSVs. As the RCLE concentration increased in the bath, a significant drop in the anodic peak current, i_a, the area under the stripping peak and oxidation waves was observed (Table T2). This finding clearly indicates that the inhibition action of RCLE is directly proportional to its concentration. The difficult oxidation and dissolution of the Ni deposited in the presence of RCLE led to a potential shift in the more noble direction. Only one anodic peak for each experiment was related to the anodic dissolution of Ni that was previously potentiostatically deposited onto the GCE. No residual metals or metal oxides were observed on the GCE beyond the anodic peak. Therefore, the charge consumed through anodic stripping can be taken as a quantitative measure of the current efficiency for Ni deposition.

3.6. Cathodic current efficiency

Cathodic current efficiency (CCE%) was achieved during Ni^{2+} electrodeposition under different operating conditions. The best conditions for Ni^{+2} electrodeposition are listed in Table T3. The CCE% value was found to be nearly 100 % under the optimal conditions. It is worth reporting that in the current studies, RCLE as an additive did not lead to any obvious decrease in the CCE% values in the Ni^{2+} electrodeposition process. Under the optimal bath conditions, bright silver Ni deposits were obtained in the presence of RCLE. It is of interest to mention that the electrolytes in this work can be used to obtain bright Ni deposits without introducing brightening agents (Table T4) compared with Ni deposited from a hydrophobic room-temperature ionic liquid, 1-butyl-1-methylpyrrolidiniumbis (trifluoromethyl sulfonyl) amide (BMPTFSA) (Zhu et al., 2014).

3.7. Surface morphology and crystal structure

SEM images and EDX patterns of the Cu substrate and Ni coatings acquired by the Watts bath are shown in Fig. 4. In both the absence and presence of RCLE, the Ni electrodeposition settings were 20 mA cm^{-2}, pH 4.5, 20 °C and t = 10 min. As shown in Fig. 4 a and a', the flat and smooth surface of the Cu substrate was deposited by the Ni coating obtained from the RCLE-free solution, Fig. 4.b.b'. The surface characteristics of the RCLE-free Ni coating exhibited a mud-like structure consisting of large grains accompanied by dimples measuring 1.5 μm in size. The presence of an unfavorable nickel deposit surface can be attributed to the simultaneous evolution of hydrogen gas, as evidenced by the analysis of cathodic polarization curves and CV results. The process of hydrogen evolution results in a decrease in the overall efficiency of the deposits. The addition of 60 μL and 100 μL of RCLE to the nickel coating resulted in significant improvements in the surface morphology, as depicted in Fig. 4.c.c' and Fig. 4.d.d', respectively. The larger grain sizes observed were 0.9 μm and 0.8 μm for the corresponding samples, whereas the Ni coated in a bath without any additives exhibited a larger grain size of 1.5 μm. The coatings exhibited enhanced smoothness, compactness, fineness, and uniformity, with crystals that were well-aligned and evenly distributed across the cathode's surface. Higher RCLE concentrations in the solution exhibited more enhanced properties of Ni deposits with finer grain sizes. Ni electrodeposition is correlated with nucleation and growth processes. The growth of Ni nuclei is limited by the presence of RCLE. This is attributed to the adsorption of RCLE molecules on low-energy surfaces, which are energetically favorable. As a result, the adsorption of RCLE molecules impedes the evolution of H_2 process, as this process can lead to the formation of pits and cracks on the surface of the deposit. Consequently, the process of RCLE adsorption results in the exclusion of low-energy surfaces, leaving only the high-energy surfaces accessible for metal deposition (Omar et al., 2020; Bani Hashemi et al., 2017). The current work successfully achieved microcracks-free nickel coatings. Previous studies have illustrated the creation of nickel deposits in Re-Ni alloys through the utilization of a combination of sodium lauryl sulfate, vanillin, and gelatin. However, the presence of micro-cracks persisted despite these efforts. These deposits were formed from aqueous solutions (Wu et al., 2016) as well as alkaline baths (Wang et al., 2019). The cracks and pits likely originated from the increased overpotential and subsequent generation of internal stress (Zhu et al., 2014). Fig. 4.a"- d" displays the characteristic EDX patterns acquired for the Cu substrate and Ni coatings, both in the absence and presence of RCLE. Before coating, a high purity of the Cu substrate was confirmed by Cu fractions of 100 %, Fig. 4.a". After coating, 93.20 % of the substrate surface was covered with Ni deposits. However, RCLE promotes the Ni fraction, Fig. 4 c",d", and enhances the surface coverage with Ni deposits to 97.32 % and 98.11 % in the presence of 60 μL and 100 μL RCLE, respectively.

More details about the coating structure can be obtained by using AFM. Three-dimensional (3D) and two-dimensional (2D) topography images and roughness parameters of the Cu substrate and the Ni coating were characterized, as shown in Fig. S4 and Table T5. The roughness parameters that were achieved in the current work are the average roughness (R_a), which gives the deviation in height, and the total roughness (R_t), which gives the vertical distance between the deepest valley and highest peak (Emran and Hanaa, 2017). The topography of the Cu substrate shows a flat surface with low R_a and R_t, as shown by 2D and 3D nuclei imaging in Fig. S4 a, a'.

The high R_a and R_t values of the topography confirmed a high roughness for the RCLE-free Ni deposit. $R_a = 66.94$ nm and $R_t = 86.91$ nm in RCLE-free Co film, Fig. S4 b.b' and Table T5. A justification for this result could be the random distribution of the grains during electrodeposition and their irregular shape due to high polarizations and coevolution of H_2, as explained in the SEM section. Adding 60 μL RCLE to the electrolyte promoted the uniformity and decreased the roughness of the Ni deposit to $R_a = 61.51$ nm and $R_t = 77.61$ nm compared to the RCLE-free Ni coating Fig. S4 c.c' and Table T5. The lowest roughness, $R_a = 40.92$ nm, $R_t = 51.63$ nm in the Ni coating, Fig. S4 d. d' and Table T5, with an increase in RCLE to 100 μL is due to more compact and uniform grain growth and their regular distribution. This result is also in good agreement with the findings obtained by visual observation from the SEM analysis. Similar behavior for glycine as a complexion agent has been obtained during Ni electrodeposition (Ibrahim and Al Radadi, 2015).

The phases of the Ni thin film as well as its crystallite size were obtained by applying XRD analysis. The typical X-ray diffraction patterns for the Cu substrate and deposited Ni films determined in the absence and presence of 100 μL RCLE are shown in Fig. 5. These patterns agree well with a face center cubic (fcc) Cu substrate (JCPDS 00–004-0836) and Ni (JCPDS 00–004-0850). The XRD patterns of the Ni crystals in the absence of RCLE exhibited a large amount of (220) and diminutive amounts of (111) and (200), as shown in Fig. 5. Most of the Ni crystallites were oriented parallel to the (220) plane because a strong (220) diffraction peak was observed at nearly 2 θ = 75.8°, indicating that (220) is the preferred growth orientation. RCLE shows a strong effect on the crystallographic orientation of the Ni crystal planes. The fcc structures of the Ni crystallites were influenced in the presence of 60 μL and 100 μL RCLE in the electrolytes, as shown in Fig. 5. The differences were in terms of the XRD peak intensity and width of the patterns. The intensity of the Ni (220) peaks dropped dramatically when RCLE was introduced in the system. However, XRD patterns exhibited diminutive amounts of fcc (200) and (111). Moreover, a slight shift in the (220) diffraction peak was observed, which indicated a decrease in the Ni crystal size with RCLE. The average crystal size for fcc (220) was estimated using the Scherrer equation. The Ni film electrodeposited in the presence of 60 μL and 100 μL RCLE showed average crystal sizes of 18.21 nm and 15.33 nm, respectively, which are smaller than that obtained from RCLE-free solution, 30.86 nm (Table T5). It has been reported that the inclusion of 1,4-bis(2-hydroxyethoxy)-2-butyne (BEO) (Deng et al., 2018), imidazole derivatives, ionic liquids (Omar et al., 2020; Omar et al., 2021) and glycine (Ibrahim and Al Radadi, 2015) as additives on the metal matrix can modify the crystal orientation.

RCLE effectively improved the microhardness of the Ni deposit. The presence of 100 μL RCLE in the Ni electrodeposition baths enhanced the Vickers microhardness Hv (kg f mm^{-2}) of the Ni coating to approximately 235.0 kg f mm^{-2} compared to 211.25 kg f mm^{-2} from RCLE-free baths (Table 4). It is worth mentioning that the microhardness of the Ni films obtained from the RCLE baths was higher than that of Ni deposited in the presence of [FPIM]Br, 213.75 kg f mm^{-2} (Omar et al., 2021); and natural Kermes dye (NKD), 225 kg f mm^{-2} (El Sayed and Ibrahim, 2019); from acidic baths.

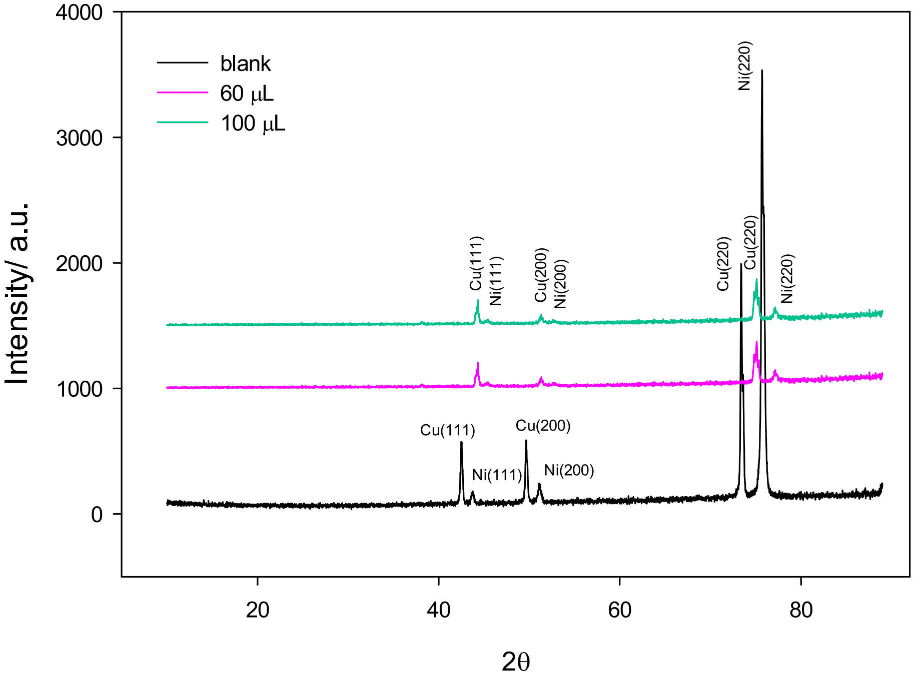

Fig. 5. XRD patterns of Cu substrate, Ni deposits in absence (blank) and presence 100 μL RCLE.

Table 4
The Vickers microhardness Hv for the Ni deposited from RCLE-free bath and the 100 μL RCLE included bath compared with some previous studies.

Additives	Hardness, H_{V100} mean ± SD	Reference
blank	211.25 ± 0.75	Current work
100 μL RCLE	235.00 ± 1.00	Current work
10^{-5} M [FPIM]Br	213.75	(Omar et al., 2021)
Natural Kermes Dye (NKD)	225.00	(El Sayed and Ibrahim, 2019)

3.8. Electrochemical impedance spectroscopy (EIS)

EIS analysis was applied to further analyze the corrosion behavior of the samples. Fig. 6.a illustrates the Nyquist plots representing the Cu substrate and Ni deposits in a 3.5 % NaCl solution, both in the absence and presence of 100 μL of RCLE. Fig. 6.c depicts the compatible equivalent circuit that corresponds to the Nyquist plots, incorporating the parameters associated with the impedance spectra. Table 5 presents the values of charge transfer resistance (R_{ct}), solution resistance (R_s), degree of roughness (n), and constant phase element (CPE). The EIS spectra obtained for nickel deposits exhibited one depressed capacitive loop, as depicted in Fig. 6.a. This characteristic feature is commonly associated with frequency dispersion, which can arise from factors such as inhomogeneity or surface roughness (Al-Fakih et al., 2019). A notable effect of RCLE is shown in the high- and low-frequency loops. The diameter of the capacitive loops for Ni deposited from RCLE-included solution was observed to be larger than that deposited from RCLE-free solution; as confirmed in Fig. 6.a and Table 5. χ^2 was approximately 1×10^{-3}-1×10^{-6}, indicating that RCLE increases the charge transfer impedance, from 7.26×10^3 kΩ cm^2 to 17.59×10^3 kΩ cm^2 of Ni deposits, as a result of a protective layer creation on the nickel deposit surfaces without modifying other factors of the corrosion behavior. A distinct diffusion behavior is clearly observed in the Ni film deposited with RCLE compared to that deposited without the RCLE additive. As shown in Table 5, the Ni deposit in the presence of RCLE exhibited the highest resistance from diffusion characterization. This corresponds to a decrease in the CPE value, suggesting a decrease in the local dielectric constant and/or an increase in the thickness of the electrical double layer. These changes can be attributed to the adsorption of additives onto the surface of the metal (Al-Fakih et al., 2019). The level of inhomogeneity (n) observed in the two metals at the interface between the film and solution was found to be ≥ 0.90, suggesting that the deposit surfaces exhibited capacitive behavior.

3.9. Potentiodynamic polarization

Fig. 6.b shows the Tafel polarization curves for Ni deposits on the Cu substrate in a 3.5 % NaCl solution both with and without 100 μL of RCLE. As shown in Fig. 6.b and Table 5, the corrosion current (i_{corr}) value exhibited a decrease, while the corrosion potential (E_{corr}) value shifted towards greater negative potentials for the nickel deposit when subjected to the presence of RCLE. The i_{corr} value decreased from 6.36×10^{-6} A cm^{-2} for the Ni deposited from an RCLE-free solution to 1.46×10^{-6} A cm^{-2} for the Ni deposited from an RCLE- solution, which indicates that the presence of the RCLE additive in the electrodeposition bath led to a higher and better corrosion resistance Ni deposit compared to that deposited from the RCLE-free solution. The result of the polarization analysis is in good agreement with the SEM, AFM and EIS measurements.

3.10. Quantum chemical calculations

Theoretical explanations for the performance of RCLE compounds as additives in the electrodeposition of nickel on a copper substrate are presented based on quantum chemical calculations of their molecular structure features. As depicted in Fig. 1, the four RCLE additives share a similar main unit structure with some variations that are regarded as the predictable active sites for cathode surface adsorption. Compound **a** is distinguished by the presence of two hydroxide groups. Compound **b** contains three hydroxide groups. Compound **c** contains both a hydroxide group and a methoxy group. Two hydroxide groups and one methoxy group are present in Compound **d.**

Fig. S5 shows the optimized molecular structures of the RCLE additives as estimated by DFT. Table 6 lists the quantum chemical parameters of the RCLE additives. The inhibitory effect of the investigated RCLE

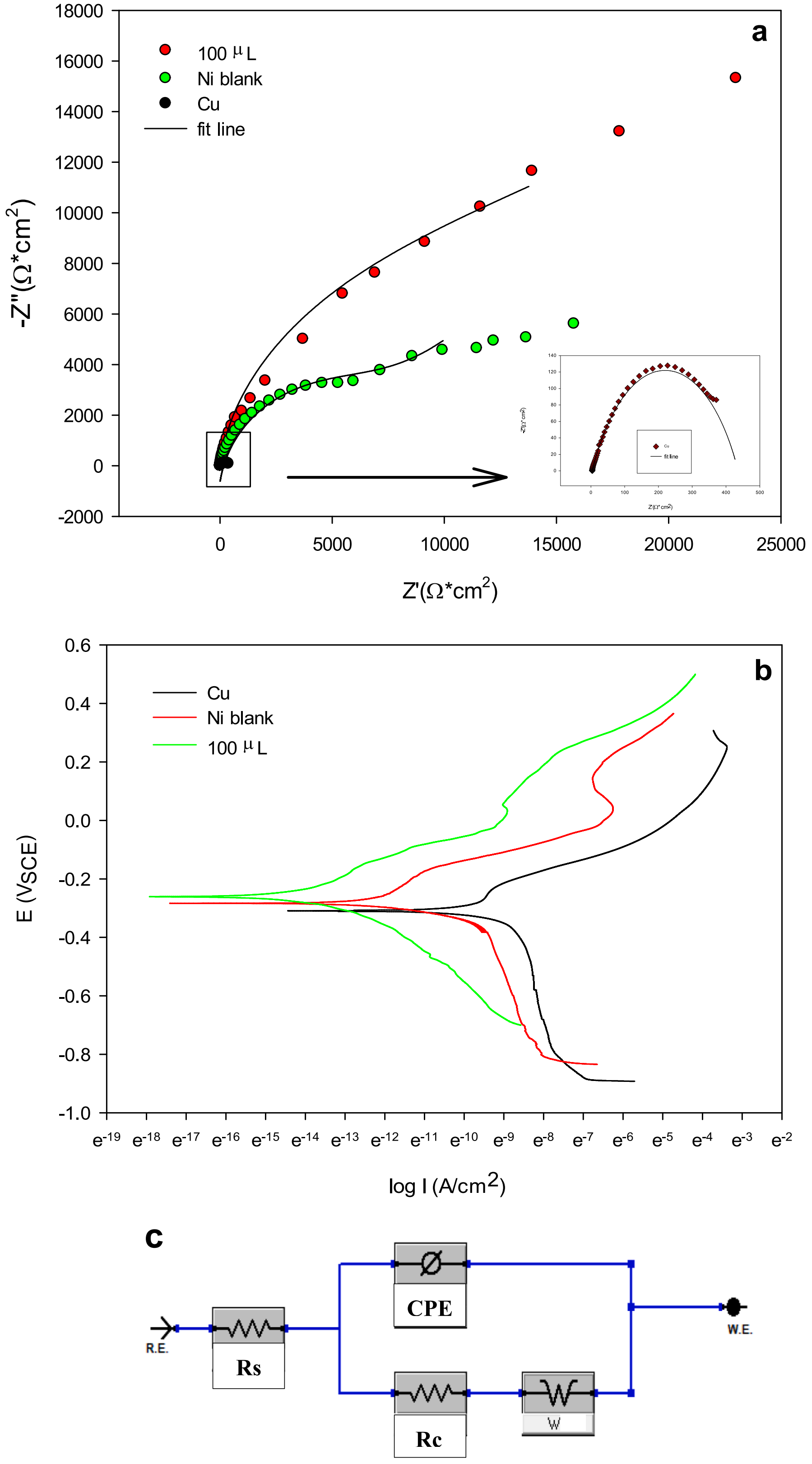

Fig. 6. (a) Nyquist plots and (b) Potentiodynamic polarization curves for Ni and Cu substrate placed in 3.5 % NaCl with and without 100 μL RCLE. (c) A circuit that is analogous to the experimental impedance data and Ni deposits.

Table 5
The impedance measurements, potentiodynamic polarization parameters for corrosion in a 3.5 % NaCl solution, and average microhardness of Ni deposits were obtained at 25 °C, both with and without the addition of RCLE.

	R_{ct} (kΩ·cm^2)	CPE (1 × 10^{-6})	n	IE%	W	i_{corr} (μAcm^{-2})	E_{corr} (mV$_{SCE}$)
Cu	4.324 × 10^2	553.70	0.6530	–	–	2.84 × 10^{-5}	−280.00
Ni blank	7.260 × 10^3	181.90	0.8880	–	627 × 10^{-6}	6.36 × 10^{-6}	−283.00
100 μL RCLE	17.590 × 10^3	114.40	0.9087	58.73	7.584 × 10^{-4}	1.46 × 10^{-6}	−360.00

Table 6
Quantum chemical parameters of RCLE additives a, b, c, and d calculated at the B3LYP/6-311++G(d,p) basis set level of DFT.

Quantum parameter	**Compound a**	**Compound b**	**Compound c**	**Compound d**
E_{HOMO}	−6.01888	−6.09943	−5.90351	−5.99575
E_{LUMO}	−1.80493	−1.92792	−1.76574	−1.88711
ΔE	4.21395	4.17150	4.13776	4.10864
I	6.01888	6.09943	5.90351	5.99575
A	1.80493	1.92792	1.76574	1.88711
χ	3.91191	4.01368	3.83463	3.94143
η	2.10697	2.08575	2.06888	2.05432
S	0.47461	0.47944	0.48335	0.48677
ΔN	0.92832	0.96216	0.92673	0.95930

compounds (IE% of 58.73 %) is attributable to their parallel adsorption on the Cu substrate surface. The parallel adsorption of these molecules can be attributed to the existence of many active sites for adsorption. The active centers in RCLE chemical structures are the hydroxide, carbonyl, and methoxy groups, as well as the π electrons of the double bond in aromatic rings. On the cathode surface, the lone pair of electrons of oxygen atoms and the electrons of the double bond of aromatic rings facilitate the adsorption of RCLE additives. As the count of double bonds rises, there is a corresponding increase in the number of π-electrons. Consequently, the facilitation of adsorption of additive molecules on the cathode surface is enhanced (Deng et al., 2018).

Fig. 7 shows the localization of HOMO and LUMO in RCLE additives. Based on research conducted on the bonding reactions and cloud distributions of organic compounds (Pramod Kumar et al., 2019), the crimson and green clouds are associated with the negative and positive phases of orbital wave functions, respectively. According to the findings presented in Fig. 7, it can be observed that the RCLE additives, namely a, b, c, and d, exhibit a notable concentration of electron density in their HOMO orbitals. This electron density is predominantly localized on the functional groups, oxygen atoms, and π electrons of the double bond. These observations suggest that the characteristic functional groups and double bonds of the RCLE additives function as electron donors. These sites represent the most preferred active sites that contribute electrons to the empty orbitals of copper atoms. The findings of this study suggest that functional groups, oxygen atoms, and π electrons are the preferred sites for the successful adsorption of RCLE additives onto the Cu substrate.

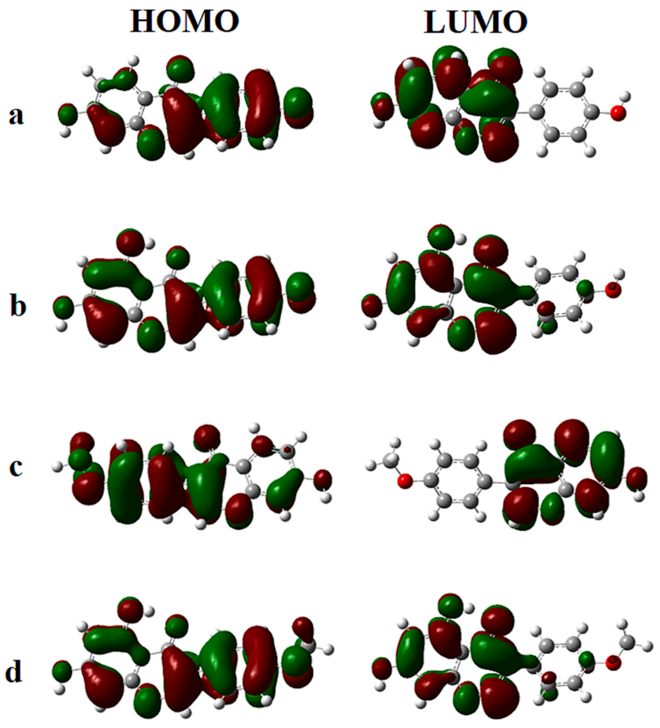

Fig. 7. Localization of HOMO and LUMO on RCLE additive molecules a, b, c, and d.

Fig. 7 displays that the electron density of LUMO distributes over the fused rings of all RCLE additives, indicating that the fused rings are the site where Cu atoms donate electrons to form back-donation bonds. These findings imply that the given electrons from the cathode surface are accepted by the atoms of the fused rings. The presence of the carbonyl as an electron-withdrawing group and the binding of multiple oxygen atoms to the fused rings may explain why LUMO distributes across the fused rings. These electron resonances on oxygen atoms result in electron deficiency on adjacent carbon atoms. As shown in Table T6 and Fig. S5, carbon atoms that are covalently bonded to oxygen have greater positive charges. The C(1), C(5), C(7), and C(9) carbon atoms on all four RCLE additive molecules and C(3) carbon atoms on Compounds b and d have greater positive charges. Due to the electron deficiency caused by the positive charges on the carbon atoms of the fused rings, LUMO is dispersed across the fused rings. These findings imply that these positively charged atoms are acceptor sites for electrons donated from the cathode surface.

According to the frontier molecular orbital theory, molecules' electron-donating and electron-accepting properties are related to the energies of their highest occupied molecular orbital (E_{HOMO}) and lowest unoccupied molecular orbital (E_{LUMO}), respectively. E_{HOMO} is associated with the molecule's electron-donating ability. Additives possessing high E_{HOMO} value have a tendency to transfer electrons to the vacant orbitals of a lower energy acceptor. E_{LUMO} is the electron-acceptance capability of a molecule (Al-Fakih et al., 2020). The value of E_{LUMO} influences the tendency for a feedback bond to form, thereby facilitating the d-orbital electron acceptance of the metal. Additives that have a lower E_{LUMO} are better at accepting electrons from the cathode surface. Stronger inhibition of Ni composite electrodeposition is caused by a longer-lasting layer of RCLE molecules adsorbing on the metal surface, which is indicated by a lower value of ΔE (Zohdy et al., 2019).

As shown in Fig. 1 and Fig. S5, the molecular structures of the four RCLE additives are nearly identical with minor differences. The difference between Compounds **a** and **b** is that Compound **b** contains an additional hydroxyl group. Furthermore, Compound **d** contains one more hydroxyl group than Compound **c**. In addition, the hydroxy group of Compounds **a** and **b** has been replaced by a methoxy group in Compounds **c** and **d**. Due to the insignificance of the differences between the molecular structures of the four compounds, there are no significant differences in the calculated quantum chemical parameters, as shown in Table 6.

3.11. Natural atomic charge (Mulliken charges)

Quantum chemical calculations were used to investigate the adsorption mode and active sites of RCLE additives based on their molecular structures. During the process of electrodeposition of copper, the presence of RCLE additives facilitates the formation of coordination bonds. These bonds are established between the unshared electron pairs of oxygen heteroatoms and the unoccupied 3d orbitals of copper atoms existing on the copper substrate. Additionally, other atoms on the additive's molecules are capable of forming back-donating bonds by accepting electrons from Cu atoms.

Table T6 displays the natural atomic charges of each atom in the RCLE molecules. The data provide mechanistic insight into the adsorption properties of the investigated RCLE additives onto the Cu substrate surface. Some elements within the molecules possess negative charges, while others possess positive charges. The oxygen atoms with the highest negative charges on these molecules are O(10), O(12), O(18), and O(19) of all four additives and O(20) of Compounds **b** and **d**. Due to the presence of unshared electron pairs, the oxygen atoms possess the highest negative charges. On all four RCLE molecules, these more negative oxygen atoms are followed by carbon atoms with less negative charges: C(2), C(4), C(6), C(8), C(13), C(14), C(16), and C(17). Additionally, C(20) on Compound **c** and C(21) on Compound **d** are negatively charged. The π bond electrons are responsible for the negative charges on the mentioned carbon atoms. These results indicate that previous atoms in the studied RCLE additive molecules have a greater capacity to donate electrons than other atoms. The vacant Cu atomic orbitals accept these electrons and serve as active sites for efficient adsorption (Pramod Kumar et al., 2019).

The largest positive charges are held by the carbon atoms C(1), C(5), C(7), C(9), and C(15) on each of the four RCLE molecules, as well as C(3) on Compounds **b** and **d**. These carbon atoms are bonded to oxygen atoms or oxygen-containing functional groups. Therefore, the highest positive charges on these carbon atoms are attributed to the resonance of the unshared electron pairs of the oxygen atoms. In light of the facts presented above, one conclusion that can be drawn is that it is beneficial to make use of quantum simulations as a technique in order to provide theoretical insights on the performance of additives in electrodeposition procedures. Quantum chemical computations can also be utilized to supplement experimental research methods.

4. Conclusion

It was possible for RCLE to effectively enhance the Ni electrodeposition from acidic sulfate baths. When compared to other RCLE concentrations, the optimal concentration of 100 μL showed a more desirable enhancement in the Ni deposit characterization, including surface morphology and mechanical and corrosion resistance qualities. High inhibition of Ni^{2+} reduction was demonstrated by a significant shift in the cathodic polarization curves toward higher negative potential values and a larger NOV value in the Ni electrodeposition in the presence of RCLE. The inhibitory effect observed on the cathode surface of RCLE can be attributed to the adsorption of four active isoflavones, namely daidzein, genistein, formononetin, and biochanin A. During Ni electrodeposition, the adsorption of active isoflavone components on the cathode surface follows the Langmuir and Temkin adsorption isotherms. The presence of RCLE in the Ni electrodeposition bath resulted in a fine-grained, reduced roughness, more compact, and greater microhardness Ni film due to the inhibition of Ni ions in the electrodeposition process as confirmed by SEM and AFM microhardness studies. The XRD spectrum showed that RCLE had no effect on the electrodeposited Ni film's crystal microstructure. According to the DFT calculations, the optimal sites for the efficient adsorption of RCLE additives on the Cu substrate during Ni electrodeposition are the functional groups, oxygen atoms, and π electrons.

CRediT authorship contribution statement

Inam M.A. Omar: Conceptualization, Data curation, Writing – original draft, Investigation, Formal analysis, Methodology. **Abdo Mohammed Al-Fakih:** Data curation, Writing – review & editing, Visualization, Investigation, Validation.

Declaration of competing interest

The authors declare that they have no known competing financial interests or personal relationships that could have appeared to influence the work reported in this paper.

Acknowledgments

The authors would like to express their gratitude to Universiti Teknologi Malaysia for supporting their research under the UTM Encouragement Research Grant [Grant no.: Q.J130000.3854.31J48].

Appendix A. Supplementary material

Supplementary data to this article can be found online at https://doi.org/10.1016/j.arabjc.2024.105680.

References

Ahamad, I., Prasad, R., Quraishi, M.A., 2010. Inhibition of mild steel corrosion in acid solution by Pheniramine drug: Experimental and theoretical study. Corros. Sci. 52, 3033–3041.

Alesary, H.F., Ismail, H.K., Shiltagh, N.M., Alattar, R.A., Ahmed, L.M., Watkins, M.J., Ryder, K.S., 2020. Effects of additives on the electrodeposition of ZnSn alloys from choline chloride/ethylene glycol-based deep eutectic solvent. J. Electroanal. Chem. 874, 114517.

Al-Fakih, A.M., Abdallah, H.H., Aziz, M., 2019. Experimental and theoretical studies of the inhibition performance of two furan derivatives on mild steel corrosion in acidic medium. Mater. Corros. 70, 135–148.

Al-Fakih, A.M., Al-Maqtari, H.M., Aziz, M., Jamalis, J., Emran, K.M., 2020. Effect of substituents on the inhibitive properties of newly synthesized 5-benzoyl-4-methyl-1,3,4,5-tetrahydro-2H-1,5-benzodiazepin-2-one derivatives against mild steel corrosion in an acidic medium. Mater. Corros. 71, 2070–2082.

Allahyarzadeh, M.H., Roozbehani, B., Ashrafi, A., 2011. Electrodeposition of high Mo content amorphous/nanocrystalline Ni–Mo alloys using 1-ethyl-3-methyl-imidazolium chloride ionic liquid as an additive. Electrochim. Acta 56, 10210–10216.

Anand Raj, M., Arumainathan, S., 2019. Comparative study of hydrogen evolution behavior of Nickel Cobalt and Nickel Cobalt Magnesium alloy film prepared by pulsed electrodeposition. Vacuum 160, 461–466.

Aribou, Z., Khemmou, N., Allah Belakhmima, R., Chaouki, I., Ebn Touhami, M., Touir, R., Bakkali, S., 2023. Effect of polymer additive on structural and morphological properties of Cu-electrodeposition from an acid sulfate electrolyte: Experimental and theoretical studies. J. Electroanal. Chem. 946, 117722.

Bani Hashemi, A., Kasiri, G., La Mantia, F., 2017. The effect of polyethyleneimine as an electrolyte additive on zinc electrodeposition mechanism in aqueous zinc-ion batteries. Electrochim. Acta 258, 703–708.

Cârâc, G., Ispas, A., 2012. Effect of nano-Al2O3 particles and of the Co concentration on the corrosion behavior of electrodeposited Ni–Co alloys. J. Solid State Electrochem. 16, 3457–3465.

Chang, Y.-J., Chen, S.-Z., Ho, C.-Y., 2015. Crystallographic structure of Ni–Co coating on the affinity adsorption of histidine-tagged protein. Colloids Surf. B Biointerfaces 128, 55–60.

Deng, S., Li, X., Fu, H., 2011. Two pyrazine derivatives as inhibitors of the cold rolled steel corrosion in hydrochloric acid solution. Corros. Sci. 53, 822–828.

Deng, J., Zhang, J., Tu, Y., Yang, P., An, M., Wang, P., 2018. Effect of BEO in the electrodeposition process of Ni/diamond composite coatings for preparation of ultra-thin dicing blades: Experiments and theoretical calculations. Ceram. Int. 44, 16828–16836.

El Sayed, M.A., Ibrahim, M.A., 2019. Natural kermes dye as an effective additive for electrochemical deposition of nickel from watts-type nickel bath. Int. J. Electrochem. Sci. 14, 4957–4973.

El-Feky, H., Negem, M., Roy, S., Helal, N., Baraka, A., 2013. Electrodeposited Ni and Ni-Co alloys using cysteine and conventional ultrasound waves. Sci. China Chem. 56, 1446–1454.

Emran, K.M., Hanaa, A.-R., 2017. Electrochemical and surface investigation of Ni-Cr glassy alloys in nitric acid solution. Int. J. Electrochem. Sci. 12, 6404–6416.

Emran, K.M., Al-Ahmadi, A.O., Torjoman, B.A., Ahmed, N.M., Sheekh, S.N., 2015. Corrosion and corrosion inhibition of cast Iron in hydrochloric acid (HCl) solution by cantaloupe (Cucumis melo) as green inhibitor. Afr. J. Pure Appl. Chem. 9, 39–49.

M.J. Frisch, G.W. Trucks, H.B. Schlegel, G.E. Scuseria, M.A. Robb, J.R. Cheeseman, G. Scalmani, V. Barone, B. Mennucci, G.A. Petersson, H. Nakatsuji, M. Caricato, X. Li, H.P. Hratchian, A.F. Izmaylov, J. Bloino, G. Zheng, J.L. Sonnenberg, M. Hada, M. Ehara, K. Toyota, R. Fukuda, J. Hasegawa, M. Ishida, T. Nakajima, Y. Honda, O. Kitao, H. Nakai, T. Vreven, J.A. Montgomery, Jr., J.E. Peralta, F. Ogliaro, M. Bearpark, J.J. Heyd, E. Brothers, K.N. Kudin, V.N. Staroverov, R. Kobayashi, J. Normand, K. Raghavachari, A. Rendell, J.C. Burant, S.S. Iyengar, J. Tomasi, M. Cossi, N. Rega, J.M. Millam, M. Klene, J.E. Knox, J.B. Cross, V. Bakken, C. Adamo, J. Jaramillo, R. Gomperts, R.E. Stratmann, O. Yazyev, A.J. Austin, R. Cammi, C. Pomelli, J.W. Ochterski, R.L. Martin, K. Morokuma, V.G. Zakrzewski, G.A. Voth, P. Salvador, J.J. Dannenberg, S. Dapprich, A.D. Daniels, O. Farkas, J.B. Foresman, J.V. Ortiz, J. Cioslowski, D.J. Fox, Gaussian 09, Revision B.1, Gaussian Inc, Wallingford, CT, 2009.

Gholami, M., Danaee, I., Maddahy, M.H., RashvandAvei, M., 2013. Correlated ab initio and electroanalytical study on inhibition behavior of 2-mercaptobenzothiazole and its thiole-thione tautomerism effect for the corrosion of steel (API 5L X52) in sulphuric acid solution. Ind. Eng. Chem. Res. 52, 14875–14889.

Gościniak, A., Szulc, P., Zielewicz, W., Walkowiak, J., Cielecka-Piontek, J., 2023. Multidirectional effects of red clover (Trifolium pratense L.) in support of menopause therapy. Molecules 28, 5178.

Guo, J., Guo, X., Wang, S., Zhang, Z., Dong, J., Peng, L., Ding, W., 2016. Effects of glycine and current density on the mechanism of electrodeposition, composition and properties of Ni–Mn films prepared in ionic liquid. Appl. Surf. Sci. 365, 31–37.

Hanini, K., Merzoug, B., Boudiba, S., Selatnia, I., Laouer, H., Akkal, S., 2019. Influence of different polyphenol extracts of Taxus baccata on the corrosion process and their effect as additives in electrodeposition. Sustain. Chem. Pharm. 14, 100189.

Ibrahim, M.A., Al Radadi, R.M., 2015. Role of glycine as a complexing agent in nickel electrodeposition from acidic sulphate bath. Int. J. Electrochem. Sci. 10, 4946–4971.

Ibrahim, M.A.M., Omar, E.M.A., 2013. Synergistic effect of ninhydrin and iodide ions during electrodeposition of zinc at steel electrodes. Surf. Coat. Technol. 226, 7–16.

Juma, J.A., 2021. The effect of organic additives in electrodeposition of Co from deep eutectic solvents. Arab. J. Chem. 14, 103036.

H. karima, B. Sameh, B. Baya, B. Louiza, H. Soraya, B. Hatem, B. Merzoug, Corrosion inhibition impact of Pyracantha coccinea M. Roem extracts and their use as additives in zinc electroplating: Coating morphology, electrochemical and weight loss investigations, Journal of the Taiwan Institute of Chemical Engineers 121 (2021) 337-348.

Kazlauskaite, J.A., Ivanauskas, L., Bernatoniene, J., 2021. Cyclodextrin-assisted extraction method as a green alternative to increase the isoflavone yield from Trifolium pratensis L. extract. Pharmaceutics 13, 620.

Kazlauskaite, J.A., Ivanauskas, L., Bernatoniene, J., 2021. Novel extraction method using excipients to enhance yield of Genistein and Daidzein in Trifolium pratensis L. Pharmaceutics 13, 777.

Kazlauskaite, J.A., Ivanauskas, L., Marksa, M., Bernatoniene, J., 2022. The effect of traditional and cyclodextrin-assisted extraction methods on Trifolium pratense L (Red Clover) extracts antioxidant potential. Antioxidants 11, 435.

Lemežienė, N., Padarauskas, A., Butkutė, B., Cesevičienė, J., Taujenis, L., Norkevičienė, E., Mikaliūnienė, J., 2015. The concentration of isoflavones in red clover (Trifolium pratense L.) at flowering stage. Zemdirbyste-Agriculture 102, 443–448.

R.T. loto, C.A. Loto, M. Akinyele, Effect of ginger, pomegranate and celery extracts on zinc electrodeposition, surface morphology and corrosion inhibition of mild steel, Alexandria Engineering Journal 59 (2020) 933-941.

Loto, C.A., Loto, R.T., 2013. Effects of Nicotiana Tobaccum extract additive on the quality of electroplating of zinc on mild steel. Pol. J. Chem. Technol. 15, 38–45.

Loto, C.A., Olofinjana, A., Popoola, A.P.I., 2012. Effect of Saccharum officinarum juice extract additive on the electrodeposition of zinc on mild steel in acid chloride solution. Int. J. Electrochem. Sci. 7, 9795–9811.

Mohanty, U.S., Tripathy, B.C., Singh, P., Das, S.C., 2002. Effect of Cd^{2+} on the electrodeposition of nickel from sulfate solutions. Part I: Current efficiency, surface morphology and crystal orientations. J. Electroanal. Chem. 526, 63–68.

Nemţoi, G., Chiriac, H., Dragoş, O., Apostu, M.-O., Lutic, D., 2009. The voltammetric characterization of the electrodeposition of cobalt, nickel and iron on gold disk electrode. Acta Chem. Iasi 17, 151–168.

Omar, I.M.A., Emran, K.M., Aziz, M., Al-Fakih, A.M., 2020. A novel viewpoint of an imidazole derivative ionic liquid as an additive for cobalt and nickel electrodeposition. RSC Adv. 10, 32113–32126.

Omar, I.M.A., Aziz, M., Emran, K.M., 2020. Part I: Ni-Co alloy foils electrodeposited using ionic liquids. Arab. J. Chem. 13, 7707–7719.

Omar, I.M.A., Al-Fakih, A.M., Aziz, M., Emran, K.M., 2021. Part II: Impact of ionic liquids as anticorrosives and additives on Ni-Co alloy electrodeposition: Experimental and DFT study. Arab. J. Chem. 14, 102909.

Omar, I.M.A., Aziz, M., Emran, K.M., 2021. Impact of ionic liquid [FPIM]Br on the electrodeposition of Ni and Co from an aqueous sulfate bath. J. Mater. Res. Technol. 12, 170–185.

Pramod Kumar, U., Shanmugan, S., Joseph Kennady, C., Shibli, S.M.A., 2019. Anti-corrosion and microstructural properties of Ni–W alloy coatings: effect of 3,4-Dihydroxybenzaldehyde. Heliyon 5, e01288.

Radadi, R.M.A., Ibrahim, M.A.M., 2021. Nickel-cobalt alloy coatings prepared by electrodeposition Part II: Morphology, structure, microhardness, and electrochemical studies. Korean J. Chem. Eng. 38, 152–162.

Rodrigues, F., Almeida, I., Sarmento, B., Amaral, M.H., Oliveira, M.B.P.P., 2014. Study of the isoflavone content of different extracts of Medicago spp. as potential active ingredient. Ind. Crop. Prod. 57, 110–115.

Saini, A., Singh, G., Mehta, S., Singh, H., Dixit, S., 2023. A review on mechanical behaviour of electrodeposited Ni-composite coatings. Int. J. Interact. Des. Manuf. (IJIDeM) 17, 2247–2258.

Santos, J.S., Matos, R., Trivinho-Strixino, F., Pereira, E.C., 2007. Effect of temperature on Co electrodeposition in the presence of boric acid. Electrochim. Acta 53, 644–649.

Saviranta, N.M., Anttonen, M.J., von Wright, A., Karjalainen, R.O., 2008. Red clover (Trifolium pratense L.) isoflavones: determination of concentrations by plant stage, flower colour, plant part and cultivar. J. Sci. Food Agric. 88, 125–132.

Schmitz, E.P.S., Quinaia, S.P., Garcia, J.R., de Andrade, C.K., Lopes, M.C., 2016. Influence of commercial organic additives on the nickel electroplating. Int. J. Electrochem. Sci. 11, 983–997.

Sorour, N., Zhang, W., Ghali, E., Houlachi, G., 2017. A review of organic additives in zinc electrodeposition process (performance and evaluation). Hydrometall. 171, 320–332.

Wang, J., Wang, Y., Xie, T., Deng, Q., 2019. Facile and fast synthesis of Ni composite coating on Ti mesh by electrodeposition method for high-performance hydrogen production. Mater. Lett. 245, 138–141.

Wojciechowski, J., Baraniak, M., Pernak, J., Lota, G., 2017. Nickel coatings electrodeposited from watts type baths containing quaternary ammonium sulphate salts. Int. J. Electrochem. Sci. 12, 3350–3360.

Wu, W., Eliaz, N., Gileadi, E., 2016. Electrodeposition of Re-Ni alloys from aqueous solutions with organic additives. Thin Solid Films 616, 828–837.

Wu, Y., Gao, Y., He, H., Zhang, P., 2019. Electrodeposition of self-supported Ni–Fe–Sn film on Ni foam: An efficient electrocatalyst for oxygen evolution reaction. Electrochim. Acta 301, 39–46.

Zaabar, A., Rocca, E., Veys-Renaux, D., Aitout, R., Hammache, H., Makhloufi, L., Belhamel, K., 2020. Influence of nettle extract on zinc electrodeposition in an acidic bath: Electrochemical effect and coating morphology. Hydrometall. 191, 105186.

Zamani, M., Amadeh, A., Lari Baghal, S.M., 2016. Effect of Co content on electrodeposition mechanism and mechanical properties of electrodeposited Ni–Co alloy. Trans. Nonferrous Met. Soc. Chin. 26, 484–491.

Zhang, Q., Hua, Y., 2009. Effects of 1-butyl-3-methylimidazolium hydrogen sulfate-[BMIM]HSO4 on zinc electrodeposition from acidic sulfate electrolyte. J. Appl. Electrochem. 39, 261–267.

Zhang, Q., Hua, Y., 2017. Ionic Liquids as Electrodeposition Additives and Corrosion Inhibitors. In: Scott, H. (Ed.), Ionic Liquids. IntechOpen, Rijeka, pp. 135–156.

Zhu, Y.L., Katayama, Y., Miura, T., 2012. Effects of acetone and thiourea on electrodeposition of Ni from a hydrophobic ionic liquid. Electrochim. Acta 85, 622–627.

Zhu, Y.L., Katayama, Y., Miura, T., 2014. Effects of coumarin and saccharin on electrodeposition of Ni from a hydrophobic ionic liquid. Electrochim. Acta 123, 303–308.

Zohdy, K.M., El-Shamy, A.M., Kalmouch, A., Gad, E.A.M., 2019. The corrosion inhibition of (2Z,2′Z)-4,4′-(1,2-phenylene bis(azanediyl))bis(4-oxobut-2-enoic acid) for carbon steel in acidic media using DFT. Egypt. J. Pet. 28, 355–359.

Zou, Z., Xu, J., Ren, W., Wang, M., Xu, Z., Wang, X., Wei, H., Huo, Y., Yu, H., 2023. Additives induced localized electrodeposition manufacturing of high quality copper micro-rectangular solid structures. J. Mater. Process. Technol. 321, 118152.